JOURNAL OF MECHANICAL ENGINEERING AND SCIENCES
ISSN: 2289-4659 e-ISSN: 2231-8380
VOLUME 19, ISSUE 2, 2025, 10604 - 10619
DOI: https://doi.org/10.15282/jmes.19.2.2025.3.0831

RESEARCH ARTICLE

Smart coating with pH-responsive micro-capsules containing corrosion inhibitors for anti-corrosion of AZ31 magnesium alloys

N. S. Mohamed[1], J. Alias[1]*, N. A. Alang[1], A. F. Omar[2]

[1] Faculty of Mechanical and Automotive Engineering Technology, Universiti Malaysia Pahang Al-Sultan Abdullah, 26600 Pekan, Pahang, Malaysia
[2] School of Physics, Universiti Sains Malaysia,11800 USM, Pulau Pinang, Malaysia
Phone: +09-4315017, Fax.: +609 431 5555

ABSTRACT - The widespread use of AZ31 magnesium (Mg) alloys in automotive, aerospace, and biomedical applications is often hindered by their high susceptibility to corrosion. In this study, a novel pH-responsive smart coating was developed, integrating multilayer microcapsules containing benzotriazole (BTA) as a corrosion inhibitor and linseed oil (LO) as a self-healing agent to enhance the corrosion resistance of Mg alloys. The BTA in the shell provides immediate corrosion protection by forming a passive barrier layer under acidic or alkaline conditions. At the same time, the LO in the core offers sustained self-healing by sealing defects over time. Dual-functional poly(urea-formaldehyde) (PUF) microcapsules were synthesized via in-situ polymerization, incorporating BTA within a chitosan-alginate multilayer shell and LO in the core. The controlled release behaviour of BTA was analysed in acidic (pH 4) and alkaline (pH 10) conditions, revealing an enhanced release profile in acidic environments, which facilitates targeted corrosion inhibition. The structural and chemical properties of the microcapsules were characterized using FTIR, UV-Vis spectroscopy, SEM-EDX, and optical microscopy. The corrosion protection performance of the smart coating was evaluated on AZ31 Mg alloy substrates using electrochemical impedance spectroscopy. The results confirmed that the smart coating significantly improved the corrosion resistance of the AZ31 Mg alloy, with film resistance (R_{film}) values of 7.211×10^4 Ω·cm² at pH 4 and 7.964×10^4 Ω·cm² at pH 10. These values are higher than those of the epoxy-coated and uncoated AZ31 Mg alloy, indicating the formation of strong passive layers that impede electrolyte penetration. The increased R_{film} shows the effectiveness of coating in enhancing corrosion inhibition and self-healing capabilities under both acidic and alkaline conditions. Overall, this study demonstrates that utilizing biodegradable, pH-responsive multilayer microcapsules is a promising and environmentally friendly approach to protecting magnesium alloys from corrosion. These results suggest that this smart coating could be a practical and environmentally friendly solution for protecting lightweight metals, particularly in vehicles and similar applications.

ARTICLE HISTORY
Received : 10th Mar. 2025
Revised : 25th May 2025
Accepted : 03rd June 2025
Published : 30th June 2025

KEYWORDS
Smart coating
Benzotriazole
Linseed oil
Magnesium alloy

1. INTRODUCTION

Corrosion presents significant global challenges, including materials safety, environmental reliability, and economic stability, with annual costs estimated at approximately US$2.5 trillion, equating to 3.4% of the global gross domestic product (GDP). Industries widely use magnesium (Mg) alloys due to their lightweight and high-strength properties. The industries' players that widely use Mg alloys are Boeing 727, Chevrolet Corvette, and orthopaedic implants [1]. However, the sensitivity of Mg alloys to corrosive media in the surrounding environment requires effective protective measures. Paints and coatings have been developed as a cost-effective and environmentally friendly solution to reduce metal degradation. Epoxy coatings are one of the preferred coatings due to their durability, chemical resistance, and cost-effectiveness. Despite these advantages, epoxy coatings often exhibit microcracks that are not visible, which can significantly impair their long-term performance by allowing the oxidation process to occur [2–4]. Latest progress has focused on enhancing the corrosion resistance of Mg alloys through the development of anti-corrosion coatings with improved adhesion, wear resistance, and environmental sustainability.

To minimize the oxidation of Mg alloys and extend their lifespan, particularly in automotive applications such as the floor and suspension components, several protective solutions have been developed over time [2, 5]. Traditional methods, such as wax, sealants, glue, and hard cover, are used in the automotive industry to prevent chipping that can lead to oxidation. However, these techniques are insufficient to provide long-term protection of the component. Recent advancements have focused on developing environmentally friendly and effective coatings to address the limitations of traditional methods. For instance, plasma electrolytic oxidation (PEO) has emerged as a promising technique, producing ceramic-like coatings that significantly enhance corrosion resistance and wear properties of Mg alloys [6]. Additionally, sol-gel coatings have gained attention due to their ability to form uniform, adherent, and corrosion-resistant layers, often

*CORRESPONDING AUTHOR | J. Alias | ✉ juliawati@umpsa.edu.my

incorporating nanoparticles to further enhance performance [7]. Moreover, the development of superhydrophobic coatings has shown the potential to reduce corrosion by minimizing water contact with the Mg alloy surface. These coatings create a water-resistant surface, thereby decreasing the chance of corrosion initiation [8]. Furthermore, research into layered double hydroxide (LDH) coatings has demonstrated their capability to act as anion-exchange materials, providing active corrosion protection by releasing inhibitive species in response to corrosive environments [9]. These innovative approaches aim to address the environmental concerns and performance limitations associated with traditional coatings, providing sustainable and efficient solutions for protecting magnesium alloys in various applications. The development of protective coatings applied to Mg alloys over the years is depicted in Table 1.

Table 1. Trend of coating applied on Mg within 10 years

Coating type	Coating constituent	Purposes	Alloy	Years	References
Plasma electrolytic oxidation (PEO) coating	Compounds calcium hydrogen phosphate dehydrate (DCPD), Octa calcium phosphate (OCP), tricalcium phosphate (TCP), and hydroxyapatite (HA)	Biomaterial	Mg alloys	2015	[10]
Microarc Oxidation (MAO/PEO) coating	Trivalent cerium (CeIII) Chitosan	Smart biomaterial	Mg-1Ca	2016	[11]
Cerium-based conversion coating	La $(NO_3)_3 \cdot 6H_2O$ or Ce $(NO_3)_3 \cdot 6H_2O$, gelatine and chitosan	Self-healing coating	AZ91D	2017	[12]
Electroless Ni coating	SiO_2 Nanocontainer (NC)/2-mercaptobenzothiazole (MBT)incorporated Ni coating	Orthopaedic implant	AZ31	2018	[13]
CO_3^{2-}-LDH conversion film	Tungstate intercalated (WO_4^{2-}—LDH) conversion film, Na_2CO_3:Mg $(NO_3)_2 \cdot 6H_2O$ and Al $(NO_3)_3 \cdot 9H_2O$	Superhydrophobic coating	AZ31B	2019	[14]
Micro arc oxidation coating	NaOH, Na_2SiO_3 and KF	Implant	AZ31	2020	[15]
Micro arc oxidation coating	Poly (1,4-butylene adipate) (PBA), isophorone diisocyanate (IPDI), dibutyltin dilaurate (DBTDL), 4′-Diamino diphenyl disulphide (DTDA)	Self-healing coating	AZ31B	2021	[16]
Epoxy resin coating	HEG-12 modified with PDA and BTA (PBG), epoxy resin	Biomaterial	AZ31	2022	[17]
PEO/PDA duplex coating	plasma electrolytic oxidation (PEO)/polydopamine (PDA)	Cytocompatibility	AZ91	2023	[18]
LDH coating	chitosan and layered double hydroxides (LDH)	Biomedical	AZ31	2024	[19]

However, the increasing environmental and health concerns regarding hazardous substances, such as Volatile Organic Compounds (VOCs), Hazardous Air Pollutants (HAPs), and Chromium (VI), have led to strict regulations and the need for eco-friendly alternatives. Chromate-free coatings have arisen from the development of Chromium-based coatings due to their highly toxic and carcinogenic nature [20]. Consequently, to improve the sustainability of Mg protection, researchers have focused on developing coatings with low VOC content, non-hazardous air pollutants, and non-toxic corrosion inhibitors [21]. To overcome the limitations of conventional coatings, smart coatings have been developed as an alternative strategy that helps prevent oxidation from occurring. These coatings not only provide passive protection but also actively respond to environmental stimuli, making them highly effective in terms of corrosion resistance [22]. The term "smart coating" refers to the functionalities of the coating that can autonomously react to environmental stimuli [23]. Smart coatings are widely used for carbon steel and steel, but are still limited for Mg alloys. Smart coatings can autonomously recover when there are changes in temperature, humidity, light, or mechanical stress, and even inhibit the growth of fouling agents such as bacteria and algae [20]. These multifunctional capabilities significantly improve material durability and performance in aggressive media and environments. The concept of smart coatings operates by sensing changes in the environment and initiating a suitable response to those stimuli [24]. They will release the active agents in a controlled manner to prevent the propagation of the cracks in the protective layer [25]. There are two types of smart coating approaches: directly incorporating inhibitors into the coating or encapsulating the inhibitors within microcapsules or nanocapsules [26]. These inhibitors require a trigger mechanism, such as changes in pH, temperature, or humidity, to control their release.

Among various trigger mechanisms, pH-responsive systems have gained attention for corrosion protection, as they can release active agents in response to localized pH changes induced by electrochemical reactions [27]. This mechanism is particularly effective for Mg alloys, which are highly prone to corrosion in chloride-containing environments. Two main approaches have been explored for developing these coatings: directly incorporating corrosion inhibitors into the coating matrix or encapsulating them within microcapsules for controlled release [26]. The latter approach, which involves multilayer polyelectrolyte microcapsules composed of chitosan and alginate, has been recognized as an environmentally friendly and efficient strategy for achieving pH-responsive corrosion protection [28,29]. Additionally, integrating film-forming agents such as linseed oil (LO) enhances the self-healing capability of these coatings by restoring the protective barrier when mechanical damage occurs [30].

An earlier study by Da Cunha et al. [28] developed dual-functional multilayer microcapsules encapsulating linseed oil, with benzotriazole (BTA) entrapped between chitosan and alginate layers to achieve both mechanical stability and pH-responsive behavior on Carbon Steel. The study revealed that BTA release was significantly higher in acidic conditions (pH $\leq$ 5) than in alkaline environments due to the pH-sensitive conformational changes of chitosan and alginate, which facilitated controlled inhibitor release at corrosion-prone sites. Furthermore, electrochemical impedance spectroscopy (EIS) demonstrated that coatings incorporating these microcapsules exhibited enhanced corrosion resistance, with higher polarization resistance ($R_{p)}$ and charge transfer resistance ($R_{c)}$ values compared to neat epoxy coatings. This suggests that incorporating pH-responsive biopolymer-based microcapsules into protective coatings offers a promising strategy for active corrosion inhibition, providing a self-healing effect while maintaining environmental sustainability. The most recent study by Flavio et al. [19] investigated a novel approach incorporating chitosan and layered double hydroxide (LDH) loaded with natural anions as corrosion inhibitors. Their findings demonstrated that the release of the kinetic inhibitor increased progressively with rising pH levels (7, 9, 10, and 11), highlighting the potential of LDH as an effective smart container for controlled inhibitor release. Among the tested coatings, the formulation containing gallate anions exhibited the highest impedance, the lowest hydrogen evolution rate, and a surface free of visible corrosion products after 21 days of exposure to a corrosive environment.

A multilayer pH-responsive polyelectrolyte system consists of alternating layers of oppositely charged polyelectrolytes that respond dynamically to fluctuations in the surrounding pH, enabling controlled release and adaptive surface properties [31]. Polyelectrolytes are charged macromolecules containing ionizable functional groups, such as amine ($-NH_3^+$) or carboxylate ($-COO^-$) groups, which dissociate in aqueous solutions to generate charged species [32], [33]. One of the most widely employed techniques for constructing multilayer polyelectrolyte films is the layer-by-layer (LbL) assembly method, which involves the sequential adsorption of oppositely charged polyelectrolytes onto a substrate through electrostatic interactions. This technique enables precise control of film thickness, composition, and functionality, making it a versatile approach for developing smart coatings [34]. The pH-responsiveness of these multilayer coatings is attributed to the ionizable groups present in the polyelectrolyte chains, which undergo protonation or deprotonation in response to variations in environmental pH [35]. These changes alter the electrostatic interactions within the multilayer structure, leading to modifications in key coating properties such as permeability, mechanical strength, swelling behaviour, and controlled release capabilities [36]. Such tuneable characteristics make multilayer pH-responsive polyelectrolyte coatings highly effective in corrosion protection applications, as they facilitate the selective and targeted release of corrosion inhibitors in response to localized pH shifts at defect sites, thereby enhancing the self-healing ability of protective coatings [37].

This study aims to investigate the interaction mechanisms of pH-responsive multilayer microcapsules within an epoxy-based smart self-healing coating for AZ31 Mg alloy. Dual-functional poly(urea-formaldehyde) (PUF) microcapsules, loaded with LO as a self-healing agent, were synthesized via in-situ polymerization. Simultaneously, pH-sensitive multilayer microcapsules containing benzotriazole (BTA), a well-established corrosion inhibitor, were developed using a layer-by-layer assembly of chitosan and alginate. The controlled release of BTA in response to pH variations enhances corrosion protection by effectively mitigating both anodic and cathodic reactions. By evaluating the effects of BTA and chitosan concentrations on the corrosion resistance and self-healing performance of multilayer smart coatings, this research provides a novel approach to improving the long-term durability of Mg alloys in harsh environments.

2. MATERIALS AND METHODS

2.1 Materials

AZ31 magnesium alloy was used as the substrate, with an elemental composition of 3 wt.% Al, 0.83 wt.% Zn, 0.31 wt.% Mn, and trace amounts of Si, Fe, Cu, and Ni, with the balance being Mg. The substrates were cut into 2 cm × 2 cm × 0.2 cm coupons using an abrasive cutter and then sequentially ground with 800- and 1200-grit silicon carbide paper. After grinding, the substrates were washed with distilled water, followed by ethanol, and dried using a cold air stream. Polyurea-formaldehyde (PUF) microcapsules were synthesized via in-situ polymerization using urea, ammonium chloride, resorcinol, polyvinyl alcohol (PVA – Mw = 40,000 g mol^{-1}, 98–99% hydrolysed), formaldehyde solution (37 wt.%), and linseed oil (LO) as the core material. Hydrochloric acid (1 wt.%) was used to adjust the pH, and all reagents were purchased from Sigma-Aldrich and used without further purification.

Multilayer microcapsules were fabricated using a layer-by-layer assembly technique with chitosan (1 mg/ml), sodium alginate (1 mg/ml), and benzotriazole (BTA). Acetic acid aqueous solution (2 wt.%), sodium hydroxide (0.1 mol L^{-1}), and hydrochloric acid (0.1 mol L^{-1}) were used to adjust the pH of the polyelectrolyte solutions. The microcapsules were subjected to repeated centrifugation and washing steps with distilled water and xylene to remove excess polyelectrolytes. The synthesized microcapsules were later incorporated into an epoxy resin coating for corrosion protection studies. Epoxy resin (D.E.R. 331) and hardener (D.E.H. 598B) were purchased from Sigma-Aldrich, both of which contained solvent levels below 0.1%, as specified in the technical sheets. The synthesized microcapsules were incorporated into the epoxy resin coating for corrosion protection studies.

2.2 Synthesis of Poly(urea-formaldehyde) Microcapsules

Poly(urea-formaldehyde) (PUF) microcapsules were synthesized via in-situ polymerization within an oil-in-water emulsion, a method extensively described and studied in the literature [28, 38, 39] . The synthesis process utilized urea, ammonium chloride, linseed oil (LO), polyvinyl alcohol (PVA, Mw 40,000 g/mol, 98–99% hydrolysed), formaldehyde solution (37 wt.%), and resorcinol, as illustrated in Figure 1. This approach enabled the formation of microcapsules with a well-defined core-shell structure, effectively encapsulating and protecting the healing agents. The in-situ polymerization method was employed to directly generate the microcapsules within the reaction medium, ensuring efficient encapsulation. Initially, 7.5 mL of a five wt.% PVA aqueous solution, serving as a stabilizer, was added to 200 mL of distilled water. While stirring at 300 rpm using a hot plate magnetic stirrer, 7.5 g of urea, 0.75 g of ammonium chloride, and 0.75 g of resorcinol were dissolved at room temperature (25–27 °C). The pH of the solution was adjusted to 3.0–3.5 by adding 1 wt.% hydrochloric acid, measured using a pH meter (Eutech Instrument). After one minute, 50 mL of LO was introduced dropwise to form a stable oil-in-water emulsion. The stirring rate was then increased to 800 rpm to regulate the microcapsule size. Subsequently, 19.02 g of a 37 wt.% formaldehyde aqueous solution was added, and the mixture was stirred for four hours at 55 °C.

Following the reaction, the emulsion was allowed to cool to room temperature (25–27 °C) for 15 minutes before being subjected to vacuum filtration using a VALUE vacuum pump. The collected microcapsules were thoroughly rinsed with distilled water and ethanol to remove residual reactants. The purified microcapsules were then dried at room temperature for 24 hours. Finally, the morphology of the dried microcapsules was examined using optical microscopy (OM).

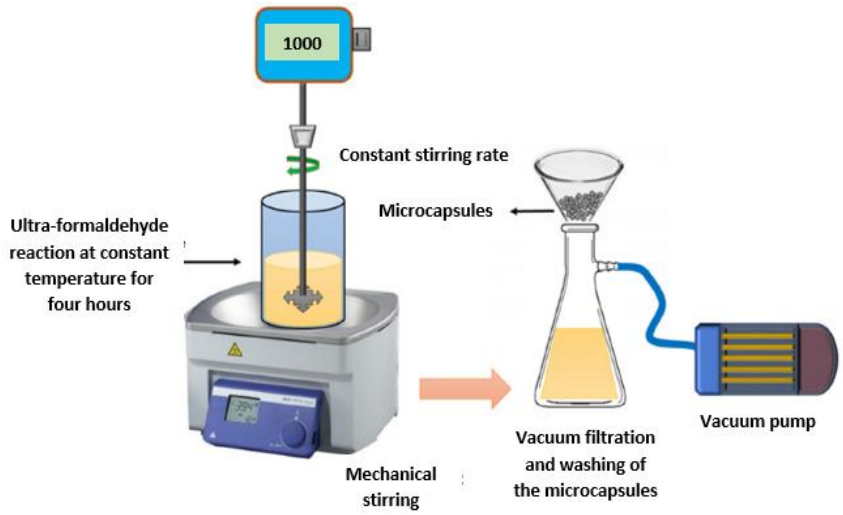

Figure 1. Schematic diagram of the experimental setup for the synthesis of encapsulated polyurea formaldehyde microcapsules

2.3 Preparation of Multilayer Microcapsules

Multilayer microcapsules were synthesized using the layer-by-layer (LbL) assembly technique, as described in [28,40]. The polyelectrolyte solution of alginate was prepared by dissolving 0.2 g of sodium alginate in 200 mL of distilled water under continuous stirring at 300 rpm using a magnetic stirrer at room temperature. Similarly, the chitosan solution was prepared by dissolving 0.2 g of chitosan in 200 mL of a 2 wt.% acetic acid aqueous solution while stirring at 300 rpm. The pH of the alginate solution was adjusted to 6.0. In contrast, the pH of the chitosan solution was set to 3.5 using either hydrochloric acid or sodium hydroxide solutions (0.1 mol L^{-1}) to ensure optimal interaction between the polycations and polyanions. Additionally, benzotriazole (BTA) was prepared by dissolving 0.1 g of BTA in a 2 wt.% acetic acid aqueous solution, with the pH adjusted to 3.5 using 0.1 mol L^{-1} hydrochloric acid to enhance its solubility. At this pH, BTA existed in its positively charged $BTAH^{+}$ form. The agitation speed during the preparation of all solutions was maintained at 300 rpm using a magnetic stirrer at a temperature of 25–27 °C. The prepared chitosan, alginate, and BTA solutions were stored in glass bottles at room temperature until further use.

Figure 2 shows microcapsule assembly via layer-by-layer deposition. First, 10 mL of the microcapsule suspension was transferred into a 50 mL centrifuge tube using a measuring cup. Upon this, 0.5 mL of 5 wt.% % chitosan solution.

The suspension was subsequently centrifuged at 2000 rpm for 2 min and then redispersed in distilled water and xylene three times to remove excess polyelectrolyte. Thereafter, 0.5 mL of alginate solution was added as the second coating layer, and the pre-coating was centrifuged and washed three times with distilled water and xylene. For the third layer, 0.5 mL of a 5 wt% polymer solution was used.% BTA solution was introduced, followed by centrifugation at 2000 rpm for 2 minutes and three washing steps. The fourth and fifth layers, consisting of alginate and chitosan, respectively, were applied using the same procedure. This sequential layering process continued until the final multilayer structure (PUF/chi/alg/BTA/alg/chi) was achieved, as depicted in Figure 2.

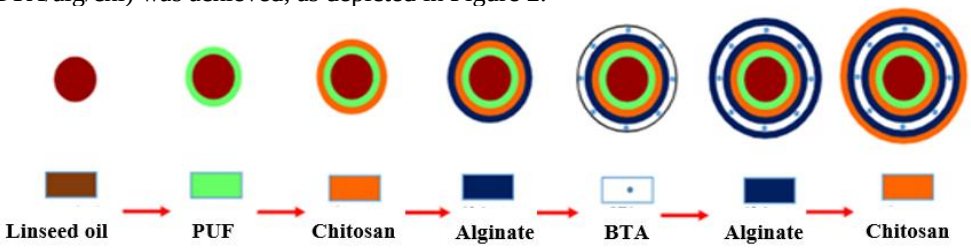

Figure 2. Schematic illustration of the assembly process of multilayer microcapsules

2.4 Characterization of Microcapsule

2.4.1 Analysis of the microcapsules without multilayer

The Fourier-transform infrared (FTIR) spectra of PUF and multilayer microcapsules were recorded using a Thermo Fisher Scientific Nicolet iS5 spectrometer to confirm the presence of functional groups within the materials. The measurements were performed over the spectral range of 4000–500 cm^{-1}, as described in the literature [19]. The FTIR spectra of chitosan and benzotriazole (BTA) were recorded prior to the experiment to confirm the presence of characteristic functional groups. As shown in Figure 3, the FTIR spectrum of BTA exhibited absorption peaks at 770 cm^{-1}, corresponding to C–H plane bending, and 3053 cm^{-1}, attributed to C–H stretching [28, 30, 41]. The peaks at 1247 cm^{-1} and 2848 cm^{-1} were assigned to N=N bending and N–H stretching, respectively. For chitosan, a strong absorption band at 3359 cm^{-1} indicated the presence of O–H groups and N–H stretching [19]. The peak observed at 2878 cm^{-1} was associated with asymmetric CH_2 stretching vibrations linked to the pyranose ring. Additionally, absorption peaks at 1594 cm^{-1} and 1649 cm^{-1} were attributed to NH_2 bending and amide I, respectively, while the peak at 1376 cm^{-1} corresponded to C–H deformation. The characteristic absorption peak at 1029 cm^{-1} confirmed C–O stretching [42,43].

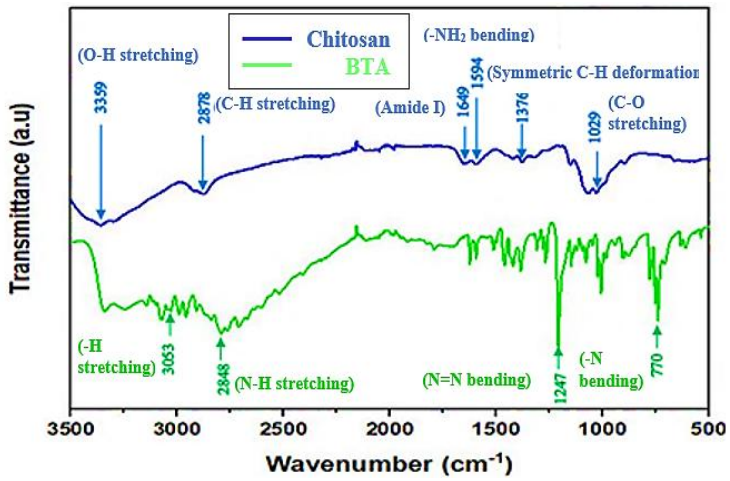

Figure 3. Fourier-transform infrared spectroscopy spectra of BTA and chitosan

2.4.2 Morphology of the microcapsules

The size and distribution of the microcapsules were analysed using an Olympus optical microscope at varying magnifications. Optical microscopy, which utilizes visible light and lenses to magnify specimens, was employed to observe the microcapsules. The powdered microcapsules were placed on a glass slide, and images were captured in bright-field mode. The acquired images were then processed using ImageJ for size analysis. Additionally, a scanning electron microscope equipped with an energy dispersive spectroscopy (SEM-EDS) was used to examine the surface morphology and composition of the microcapsules. High-resolution imaging and elemental analysis were performed using a JEOL SEM in high-vacuum mode, with an acceleration voltage of 10 kV and a working distance of 9.8 mm. Prior to imaging, the sample was gold-coated to prevent surface charging.

2.4.3 Analysis of the pH response

The pH-responsive behaviour of the multilayer microcapsules was evaluated using an Ocean Optics QE65000 spectrometer connected to a computer. The absorbance spectra of the microcapsule solutions were recorded immediately

after synthesis in buffer solutions at pH 4 and 10 [44–46]. For the release experiment, 0.04 g of multilayer microcapsules was dispersed in a buffer solution and subjected to ultrasonic radiation for 5 minutes using a Sonics Vibra-Cell CV18 sonicator. After immersion, 3 mL of the mixture was collected and transferred into a cuvette. Absorbance measurements were conducted at wavelengths ranging from 220 nm to 400 nm for 3 hours at 25 °C [47–49]. The spectra were analysed using SpectraSuite® software, with an integration time of 8 seconds, which defines the duration during which the spectrometer collects photons.

2.5 Preparation of the Epoxy Coating

To fabricate the epoxy-based smart coatings, 0.3 g of microcapsules with all three types were accurately weighed using an electronic balance. Four types of specimens are prepared: bare AZ31 Mg substrate, AZ31 Mg substrate coated with pure epoxy resin, AZ31 Mg substrate coated with PUF microcapsules, and AZ31 Mg substrate coated with epoxy resin containing 10 wt.% multilayer microcapsules [28, 50]. The epoxy was prepared by mixing 3 g of Epoxy E101 with 1 g of Hardener H181 in a 3:1 ratio, as recommended by the manufacturer. The resulting combination was stirred with a glass rod, and in turn, PUF and multilayer microcapsules were added to form the coatings. A pure epoxy coating was also made in the same manner, excluding microcapsules. The coats were then deposited onto the Mg substrate with a film thickness of 100 µm, consistently using a thin-film applicator, and dried at room temperature for 48 hours. The coating of nine samples was performed, and the results are summarized in Table 2.

Table 2. Electrochemical parameters of multilayer smart coatings in acidic buffer solution (pH 4), determined by fitting EIS data

Sample Number	Chitosan Concentration (wt.%)	BTA Concentration (wt.%)
S1	5	5
S2	10	5
S3	5	10
S4	10	10
S5	5	15
S6	10	15
S7	PUF coated	
S8	Epoxy coated	
S9	Bare Mg	

2.6 Corrosion Performance Analysis

Electrochemical impedance spectroscopy (EIS) was performed using a Gamry Interface 1000E potentiostat/galvanostat equipped with a three-electrode system, consisting of the sample as the working electrode, a graphite rod as the counter electrode, and an Ag/AgCl electrode as the reference electrode. The tests were conducted in an aqueous buffer solution at pH four and pH 10 to complement the release studies. Each measurement was repeated three times to ensure accuracy and reproducibility. The EIS test was performed with the following parameters: a DC voltage of 0 V was applied, and the frequency range was set from 100,000 Hz to 0.01 Hz, at 10 points per decade [50]. The DC voltage modulation was set to 5 mV/m. The sample area was 4 cm^2, and the estimated impedance was 1000 Ω. The measurements were optimized for normal noise conditions to ensure accuracy and minimize interference. The EIS data were fitted using the ZView Software.

3. RESULTS AND DISCUSSION

3.1 FTIR Analysis of the Microcapsules

Fourier Transform Infrared Spectroscopy (FTIR) analysis of PUF microcapsules revealed the encapsulation of linseed oil within the PUF shell, as depicted in Figure 4. The FTIR spectrum showed a strong absorption band at 3340 cm^{-1} due to the stretching vibration of O-H and N-H, and an absorption band at 1657 cm^{-1} due to the stretching vibrations of C=O. These spectral contributions were in agreement with the nature of the PUF microcapsule walls as determined previously [28]. Moreover, the FTIR spectrum also displayed certain characteristic peaks of linseed oil, absorption peaks at 2924 cm^{-1} for =C-H stretching, 2852 cm^{-1} for C-H stretching, 1461 cm^{-1} for C-H bending, 1746 cm^{-1} for C=O stretching, and 1167 cm^{-1} for C-O stretching. These results again proved the successful encapsulation of linseed oil in PUF Microcapsules using in situ polymerization. The microcapsules were thoroughly rinsed with xylene and distilled water before analysis to eliminate residual impurities.

The FTIR spectrum of BTA in multilayer microcapsules had an absorption peak at 773 cm^{-1}, and it is ascribed to the C-H plane bending and C-H out-of-plane bending vibration of the benzotriazole benzene ring [41]. Another significant peak was observed at 2840 cm^{-1}, which is the stretching vibration of the benzene ring, triazole ring, and N-H stretching in multilayer microcapsules [19]. The FTIR spectrum of chitosan exhibited a peak at 2850 cm-1 corresponding to the asymmetric CH_2 stretching vibrations of the pyranose ring. Furthermore, the absorption peak at 1640 cm^{-1} was attributed

to amide I, whereas the peak at 1250 cm^{-1} could be the N=N stretching, which would belong to multilayer microcapsules [19]. The broad absorption band at 3320 cm^{-1} (O-H, N-H overlapping band) was assigned to the presence of PUF in the multilayer microcapsules.

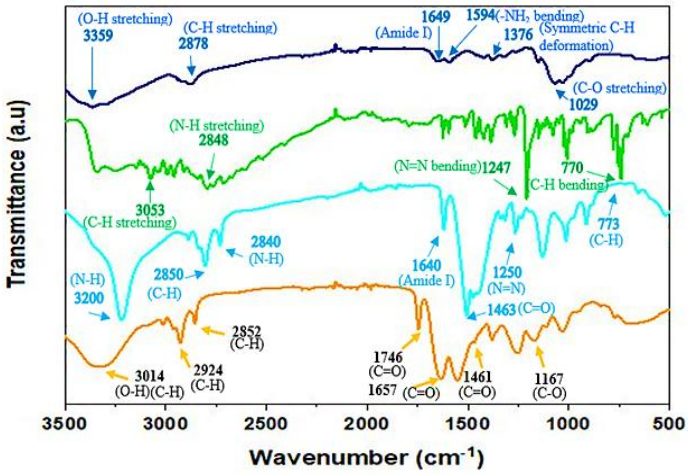

Figure 4. FTIR analysis of chitosan, BTA, multilayer microcapsules, and PUF microcapsules

3.2 Morphology of the Microcapsules

The successful synthesis of encapsulated microcapsules and multilayer biopolymer microcapsules was achieved. Optical microscopy (OM) and scanning electron microscopy (SEM) were used to analyse morphology and determine the size of linseed oil-filled and multilayer microcapsules. Figure 5 presents SEM and OM images of synthesized PUF microcapsules, while Figure 6 displays microcapsules with chitosan/alginate/BTA/alginate/chitosan multilayers. The PUF microcapsules in Figure 5(a) exhibit a spherical, non-porous, mononuclear structure [28, 39]. Their rough surface morphology, shown in Figure 5(b), likely results from interactions between inhomogeneous reaction kinetics, fluid-induced shear forces, and shell elasticity. This coarse surface is expected to enhance adhesion to the coating matrix, improving self-healing coating performance [39].

Figure 5(c) presents microcapsules with irregular shapes, where the core material is fragmented and embedded within various wall structures. Encapsulation occurs due to liquid-phase separation, followed by the polymerization of urea and formaldehyde, leading to the formation of a low-molecular-weight prepolymer in an aqueous solution. The accumulation of polymer at the organic/aqueous interface is attributed to the presence of formaldehyde monomers. The polymerization process, facilitated by resorcinol and ammonium chloride, strengthens the urea-formaldehyde capsule walls [38]. As shown in Figure 5(d), the precipitation of high-molecular-weight prepolymers confirms the formation of PUF microcapsules.

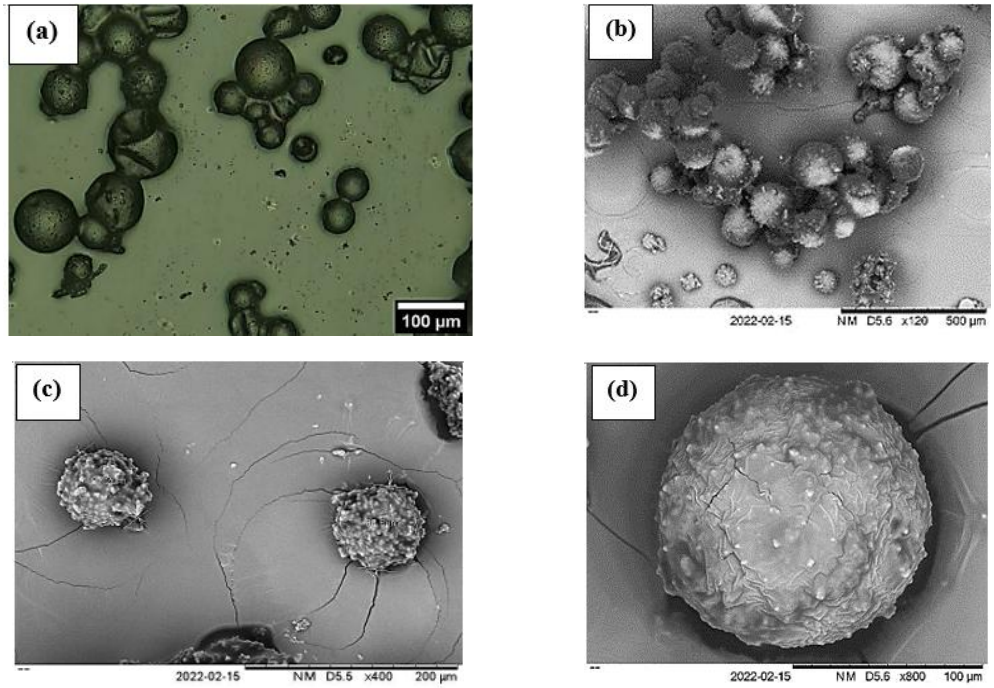

Figure 5. (a) Optical microscopy image of PUF microcapsules and (b-d) Scanning electron microscopy images of PUF microcapsules

Figure 6 illustrates the surface morphology and chemical composition of multilayer microcapsules for S1 (5 wt.% chitosan, 5 wt.% BTA). As shown in Figure 6(a), the microcapsules appear as a creamy-coloured powder, while Figure 6(b) reveals significant agglomeration. This agglomeration is primarily attributed to the adhesive nature and insolubility of chitosan, along with the tendency of micrometric-sized particles to cluster to minimize surface energy [51,52]. Although the particles remain stable in dispersion, the drying process further intensifies agglomeration. Figure 6(c) demonstrates that the multilayer microcapsules exhibit a nearly spherical shape with an aggregated distribution. In contrast, PUF microcapsules display a more uniform spherical morphology, with an average size of approximately 11.25 µm. Energy-dispersive Spectroscopy (EDS) analysis (Figures 6(d–g)) confirms the elemental composition of the microcapsules, identifying carbon (80.57 wt.%), nitrogen (0.77 wt.%), and oxygen (18.66 wt.%).

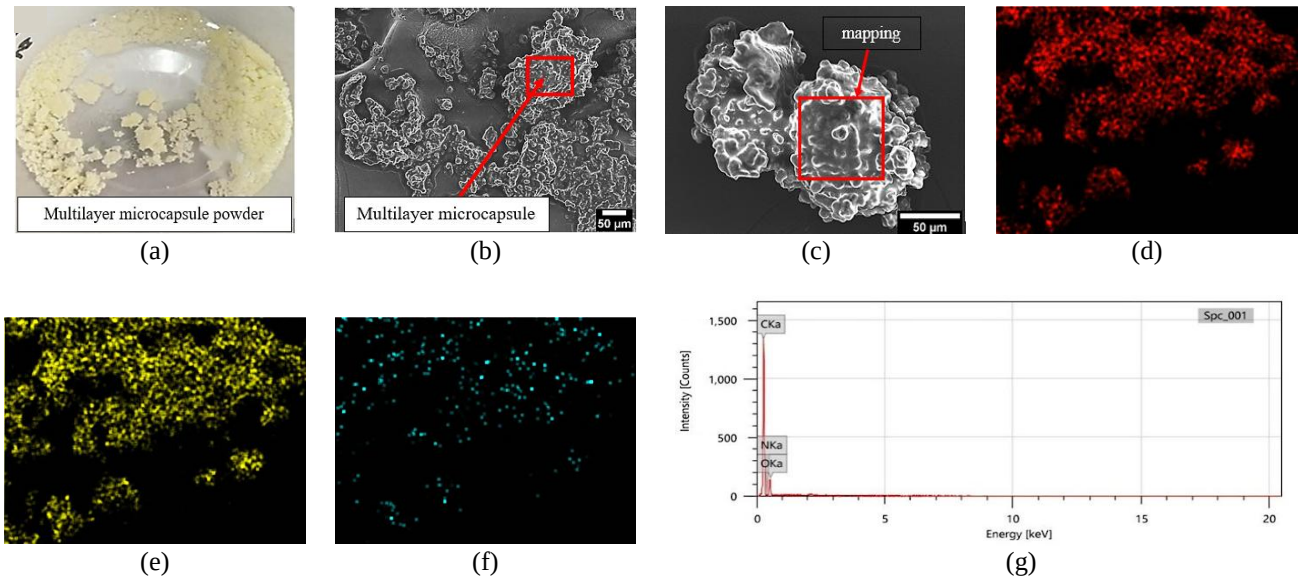

Figure 6. Microcapsule characterization: (a) Optical image of dried multilayer microcapsules for S1, (b) SEM image of multilayer microcapsules at 200× magnification, (c) SEM image of multilayer microcapsules at 500× magnification, (d–f) EDS elemental mapping of C, N, and O, and (g) EDS spectrum analysis

3.3 Analysis of the pH Response

The BTA release profiles of six different microcapsule formulations (S1–S6) were evaluated under acidic (pH 4) and alkaline (pH 10) conditions over time to assess their structural integrity and permeability. The results indicate distinct release behaviours influenced by environmental pH. At pH 4, the BTA-released rate of all formulations exhibited an initial rapid growth process, reaching a peak value within the first 60 minutes. This burst release indicates the existence of the BTA, which was either loosely adsorbed or bound to the surface of the EM/R graphene and rapidly diffused into the surrounding solution. Second-stage distribution trends differed as expected after the first one. S1 and S6 sustained-release behaviours were observed, with S6 exhibiting the highest cumulative percentage of BTA release greater than 60% at 180 minutes. This phenomenon indicates a relatively permeable or degradable microcapsule structure of S6 in an acidic environment. On the other hand, the release of S3 and S4 decreased after 60 minutes, perhaps due to re-adsorption, decomposition, or instability of the microcapsule walls with prolonged exposure [28]. Those of S2 and S5 were consistently low and, at BTA, diffused at a modest amount over time, indicating a controlled release [54]. It has been suggested that differences in multilayer composition, cross-linking density, and wall porosity account for the observed differences in release kinetics [55]. These results indicate that S6-type formulations may be more promising for the long-term release of BTA in an acidic environment compared to S3 and S4 types, which may require further development to prevent premature degradation and ensure controlled release.

Under alkaline conditions (pH 10), the BTA release behaviour differed significantly. All formulations exhibited an initial increase in BTA release within the first 60 minutes, followed by a phase of stabilization. However, the maximum release was considerably lower than that observed under acidic conditions, with values not exceeding 25%. This trend suggests that the microcapsule walls exhibit higher stability in an alkaline medium, effectively limiting the diffusion of the encapsulated BTA [53]. Among the formulations, S5 and S2 displayed the highest release levels, reaching approximately 22%, while S1 and S6 exhibited the lowest release, remaining below 15% throughout the experiment. The restricted BTA release in alkaline conditions may be attributed to the reduced solubility of the multilayer components or strengthened electrostatic interactions that hinder diffusion [54]. The relatively stable release profiles beyond 60 minutes indicate a controlled and sustained release mechanism in an alkaline environment. Together, these data indicate that the microcapsule formulations efficiently control BTA release, depending on the pH environment. The high release at pH 4 indicates the suitability of these microcapsules for sustained BTA diffusion applications under acidic conditions. In contrast, the low level of release at pH 10 highlights their stability at basic pH, resulting in minimal premature release. For applications requiring faster release rates under basic conditions, additional modification of the multilayer composition may be necessary to increase the system's permeability while maintaining its structural integrity. These

results provide important information for the development and optimization of microcapsules for the controlled release of BTA in various pH environments.

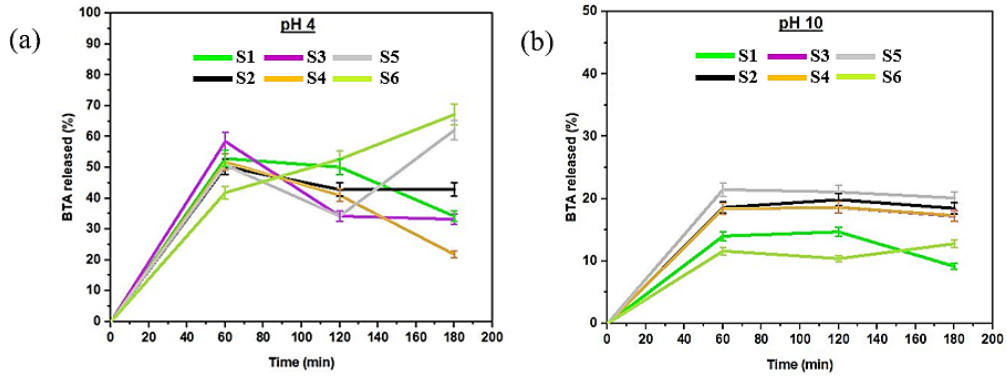

Figure 7. BTA release profile from multilayer microcapsules in buffer solutions at: (a) pH 4 and (b) pH 10 over a 3-hour duration

The release rate of BTA observed in this study surpasses previous reports [55]. The release profile by [56] for Mg AZ31 demonstrated a 44% increase in corrosion inhibitor release in an acidic medium over the first 10 hours. The release is pH-dependent, with higher pH values leading to lower inhibitor release, thereby slowing the active response to corrosion. This behaviour is primarily influenced by the pH-responsive nature of chitosan in the multilayer microcapsule system. Under acidic conditions (pH 4), chitosan undergoes protonation, resulting in electrostatic repulsion between its chains, which expands the polymer's structure. This expanded conformation enhances the accessibility of hydrogen ions (H^+) to the alginate layer, thereby promoting interaction and facilitating the release of BTA. Chitosan, derived from chitin, contains amine functional groups ($-NH_2$) that become protonated in acidic environments, forming positively charged amino groups ($-NH_3^+$), as shown in Figure 8. However, in alkaline conditions (pH 10), deprotonation occurs, where amino groups lose protons, resulting in neutral $-NH_2$ groups [57]. Similarly, alginate, composed of mannuronic and guluronic acid units, exhibits pH-sensitive behaviour. In acidic conditions, its carboxyl groups (-COOH) undergo protonation, enhancing BTA release due to the preferential interaction of alginate with H^+ ions. In contrast, under alkaline conditions, deprotonation leads to the formation of carboxylate ions ($-COO^-$), reducing H^+ interaction and consequently restricting BTA release [58], [59]. At pH 10, the higher concentration of hydroxyl ions (OH^-) causes the chitosan chains to collapse, reducing the interaction between alginate and hydrogen ions and thereby inhibiting BTA diffusion. This structural transformation is depicted in Figure 8 [60, 61]. These findings highlight the crucial role of chitosan and alginate in regulating BTA release in response to environmental pH, making them effective components in pH-responsive corrosion protection systems.

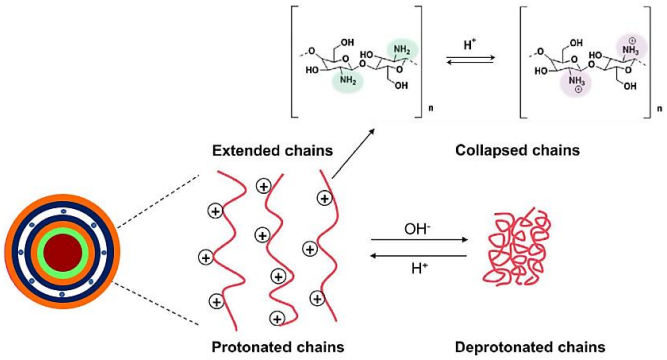

Figure 8. The schematic illustration depicts the various conformations of the chitosan layer in response to pH variations

3.4 Corrosion Performance Analysis

Figure 9 shows the electrical equivalent circuits of the impedance response of both the magnesium alloy substrate and the multilayer smart coating in the acidic medium (pH 4). Figure 9(a) depicts the bare Mg alloy, and the electrochemical system is generally simulated by R_{sol}, along with a parallel circuit consisting of the charge transfer resistance of the magnesium substrate (R_{Mg} substrate) and the double-layer capacitance (C_{Mg} substrate). This simplified circuit arrangement illustrates the interaction of the magnesia substance with the Mg substrate, resulting in rapid corrosion due to its lack of a protective covering. In comparison, the equivalent circuit of the multilayer smart coating, as shown in Fig. 9(b), is more complex due to the presence of additional impedance elements associated with the protective coating and passive film formation. The circuit consists of R_{sol}, then the parallel R_{coat} and the constant phase element of the coating (CPE_{coat}), which is sensitive to the dielectric and barrier properties of the coating. Furthermore, the existence of R_{film} and CPEfilm indicates the formation of an intermediate protective film on the film surface, which may result from the self-healing behavior or the release of corrosion inhibitors.

The third part of the equivalent circuit, R_{ct}, is related to the charge transfer resistance at the metal-coating interface, which is significantly greater in well-protected samples, indicating higher corrosion resistance. The EIS findings in Table 3 are consistent with this circuit model, indicating that coated samples (S1–S8) with varying values of R_{coat}, R_{film}, and R_{ct} exhibit different levels of coating integrity and inhibitor efficiency. As for the S9 group, the R_{ct} value was much higher, indicating a delivery against passive layer formation, as shown in Figure 9(b). In contrast, samples with lower R_{coat} and R_{ct} values exhibit similar barrier performance to the uncoated Mg alloy, as shown in Figure 9(a). The above results demonstrate the potential of multilayer smart coatings to prevent corrosion by introducing additional electrochemical obstacles that retard the ingress of electrolyte and charge transfer, ultimately enhancing the long-term stability of the Mg alloy [27].

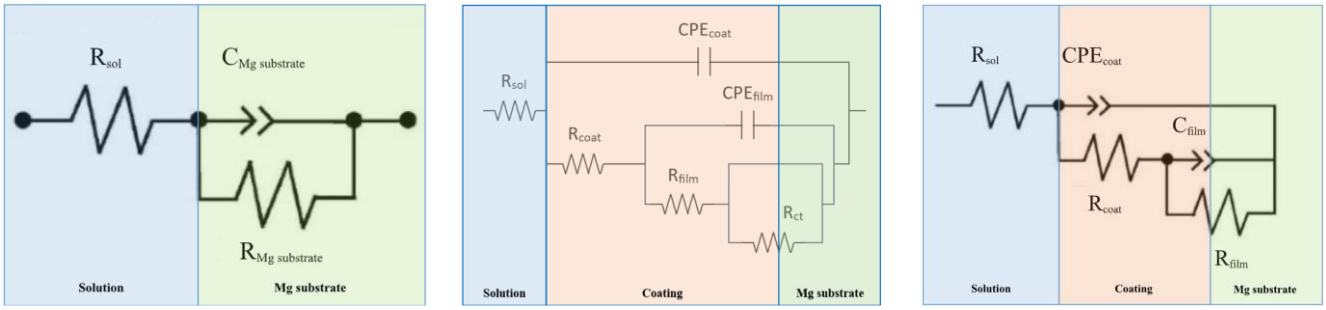

(a) (b) (c)

Figure 9. The electrical equivalent circuit is presented for: (a) the bare Mg alloy, the multilayer smart coating immersed in buffer solution, (b) pH 4, and (c) pH 10

The electrochemical impedance spectroscopy (EIS) fitting data in Table 3 quantifies the corrosion resistance of multilayer smart coatings in an acidic buffer solution (pH 4). Among the tested samples, S2 exhibited the highest R_{film} value, measuring 7.211×10^4 Ω·cm². S1 exhibited a film resistance of R_{film} (0.673×10^3 Ω·cm²) and low capacitance, suggesting minimal electrolyte penetration. S3 demonstrated the second-highest resistance R_{coat} (3.737×10^3 Ω·cm²), confirming strong protective properties [62], whereas S4 showed a lower R_{coat} (0.656×10^3 Ω·cm²), suggesting moderate corrosion resistance. S5 and S6 displayed reduced resistance values R_{coat} (3.838×10^3 Ω·cm² and 1.081×10^3 Ω·cm², respectively), indicating limited anti-corrosion performance due to increased electrolyte penetration. S7 and S8 exhibited the weakest corrosion resistance, with S7 recording the lowest R_{coat} among coated samples (1.489×10^3 Ω·cm²), followed by S8 (0.824×10^3 Ω·cm²), confirming rapid degradation in acidic conditions. As expected, the bare AZ31 magnesium alloy (S9) exhibited the poorest performance, with R_{ct} (17.6 Ω·cm²), reinforcing its high susceptibility to corrosion without a protective coating. These findings emphasize the importance of optimized coating formulations in enhancing corrosion resistance, where S2 demonstrated the most effective protection. At the same time, S8 and S9 exhibited the least resistance, highlighting the need for further improvements in coating design for aggressive environments. The study by [48, 63, 64] shows that the value of R_{film} is higher for all microcapsule-coated samples that contain corrosion inhibitors.

Table 3. The electrical parameters were determined by fitting EIS data to an acidic buffer solution (pH 4)

Sample	Rs_{ol} (Ω cm²)	R_{coat} (Ω cm²)	CPE_{coat} (F/cm²)	R_{film} (Ω cm²)	CPE_{film} (F/cm²)	R_{ct} (Ω cm²)
S1	0.153×10^3	1.218×10^3	1.852×10^{-4}	0.673×10^3	4.24×10^{-4}	0.462×10^3
S2	0.170×10^3	1.458×10^3	1.879×10^{-4}	7.211×10^4	7.335×10^{-5}	0.985×10^3
S3	0.377×10^3	3.737×10^3	6.255×10^{-5}	2.857×10^4	2.557×10^{-5}	1.283×10^3
S4	0.257×10^3	0.656×10^3	3.439×10^{-5}	1.353×10^3	2.717×10^{-4}	1.368×10^3
S5	0.210×10^3	3.838×10^3	1.020×10^{-7}	3.838×10^3	2.66×10^{-10}	0.778×10^3
S6	0.162×10^3	1.081×10^3	3.357×10^{-4}	0.813×10^3	4.633×10^{-4}	0.065×10^3
S7	0.350×10^3	1.489×10^3	5.094×10^{-8}	2.633×10^3	3.346×10^{-4}	0.509×10^3
S8	0.360×10^3	0.824×10^3	1.563×10^{-3}	0.524×10^3	2.391×10^3	0.339×10^3
S9	0.037×10^3	-	-	-	-	17.6

The EIS parameters for pH 10 reveal notable variations in the protective capabilities of different coatings. Sample S1 exhibits the highest R_{coat} (2.022×10^4 Ω cm²), indicating superior barrier properties and enhanced corrosion resistance [44, 50]. This is further supported by its relatively low CPE_{coat} value (4.074×10^{-7} F/cm²), suggesting limited electrolyte penetration and improved coating stability. Additionally, R_{film} for S1 (7.239×10^3 Ω cm²) confirms the formation of an effective passive film, further mitigating corrosion activity. A similarly high R_{coat} value (8.795×10^3 Ω cm²) was observed for S8, suggesting another well-performing coating system with strong resistance to corrosive attack. Conversely, coatings in S2 and S3 exhibit significantly lower R_{coat} values (1.511×10^3 Ω cm²), indicating weaker protective properties. Their relatively higher CPE_{coat} values reflect increased electrolyte uptake, which may compromise long-term durability. The intermediate film resistance (R_{film}) varies across samples, with S4 (7.964 × 10^4 Ω cm²) and S6 (6.288 × 10^3 Ω cm²) displaying strong passive layer formation, which aligns with their moderate R_{coat} values. As expected, Sample S9,

representing the uncoated Mg alloy, lacks any protective coating (R_{coat} not applicable) and exhibits the lowest R_{film} (0.134 × 10^3 Ω cm^2), indicating severe corrosion susceptibility in alkaline conditions. The exceptionally high CPE_{film} value (1.344 × 10^{-4} F/cm^2) further confirms increased charge accumulation due to direct electrolyte interaction with the exposed substrate.

Table 4. The electrical parameters were determined by fitting EIS data to an alkaline buffer solution (pH 10)

Sample	Rs_{ol}(Ω cm^2)	R_{coat}(Ω cm^2)	CPE_{coat}(F/cm^2)	R_{film}(Ω cm^2)	CPE_{film}(F/cm^2)
S1	0.661 x 10^3	2.022 x 10^4	4.074 x 10^{-7}	7.239 x 10^3	8.870 x 10^{-8}
S2	0.225 x 10^3	1.511 x 10^3	1.999 x 10^{-9}	4.131 x 10^4	1.894 x 10^{-7}
S3	0.572 x 10^3	1.511 x 10^3	6.566 x 10^{-10}	1.589 x 10^4	2.009 x 10^{-6}
S4	0.339 x 10^3	5.242 x 10^3	4.384 x 10^{-8}	7.964 x 10^4	2.586 x 10^{-9}
S5	0.155 x 10^3	1.94 x 10^5	6.475 x 10^{-8}	1.475 x 10^4	2.771 x 10^{-3}
S6	0.894 x 10^3	4.362 x 10^4	1.601 x 10^{-8}	6.288 x 10^3	7.001 x 10^{-8}
S7	0.724 x 10^3	4.478 x 10^3	3.166 x 10^{-10}	7.374 x 10^3	1.104 x 10^{-9}
S8	0.407 x 10^3	8.795 x 10^5	7.500 x 10^{-11}	0.196 x 10^3	3.602 x 10^{-9}
S9	0.163 x 10^3	-	-	0.134 x 10^3	1.344 x 10^{-4}

Figure 10 Nyquist diagram of sample S1 (a) The highest charge-transfer resistance of 6.0 kΩ·cm^2 among all samples was observed (b), indicating better corrosion resistance in acidic medium. The two-time constant behaviour demonstrates that coating and substrate-related resistances are present, indicating an efficient barrier mechanism [65]. Sample S2 had an intermediate impedance of 5.4 kΩ·cm^2. Its capacitive loop has a larger diameter than the S1 sample, indicating good coating resistance [66]. However, it is slightly lower than the S1 one. For Sample S3, it has an impedance of 7.0 kΩ·cm^2 and a much larger capacitive loop diameter, which demonstrates excellent corrosion resistance. In contrast, the impedance of Sample S4 was 3.5 kΩ·cm^2, which indicates the inferior protective performance relative to that of Sample S3, as presented in Figure 10(b). Samples S5 and S6 were not as successful, with sample S6 presenting the lowest impedance at 1.8 kΩ/cm^2 (Figure 10c). The double capacitive loops observed in the present samples suggest two capacitance components: one corresponding to the high-frequency coating properties and the other to the low-frequency electrochemical reaction under the coating [65]. Similar observations have been reported by other researchers [65].

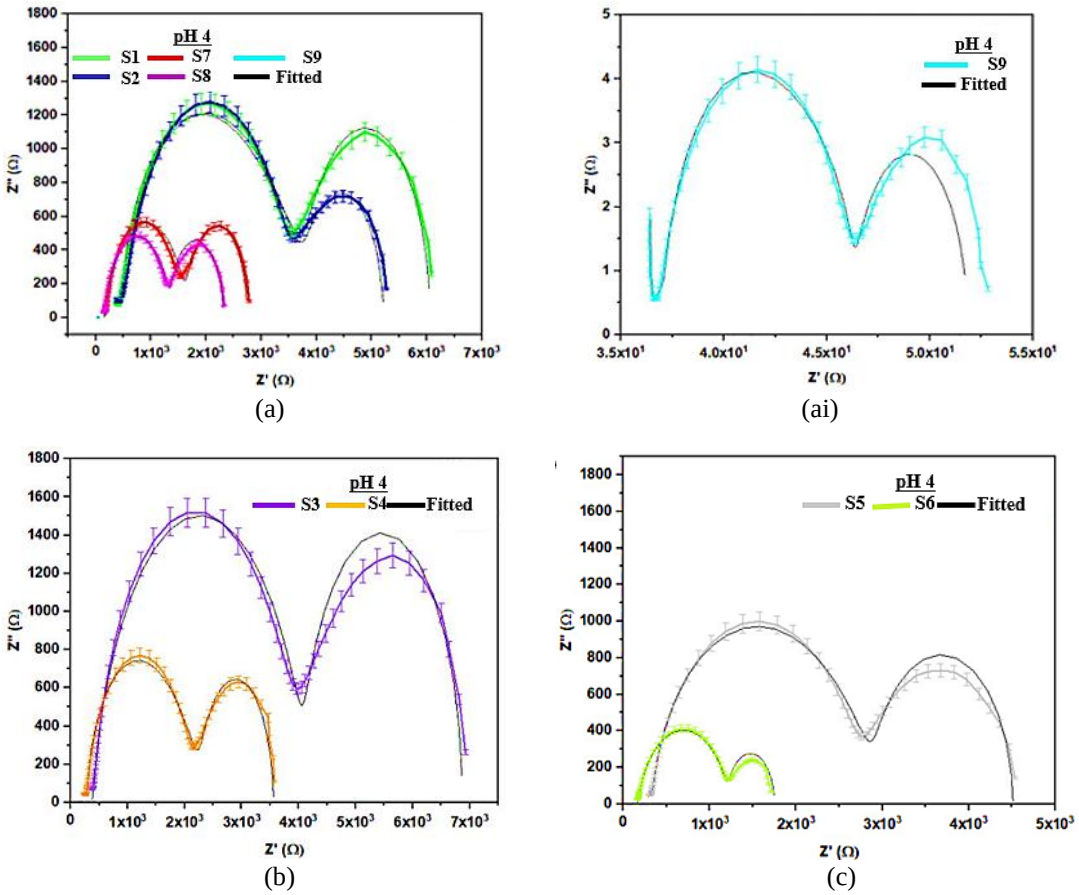

Figure 10. The Nyquist plot of the coated sample in pH 4: (a) S1, S2, S7, S8, S9, (ai) magnified Nyquist plot of S9, (b) S3 and S4, and (c) S5 and S6

Samples S7 and S8 exhibited significantly lower impedance values, with Sample S8 having a value of 2.3 kΩ·cm². The compressed semicircle diameters in these samples indicate higher corrosion susceptibility, suggesting faster degradation or increased electrolyte penetration, leading to reduced barrier properties. The bare AZ31 Mg alloy (S9) exhibited the lowest impedance at 0.03 kΩ·cm², indicating its high susceptibility to corrosion in acidic environments. Overall, the impedance data confirm that multilayer smart coatings enhance corrosion resistance in acidic environments.

Electrochemical impedance spectroscopy (EIS) analysis at pH 10 revealed distinct variations in corrosion resistance among the multilayer smart coating samples. Figure 11(a) illustrates the experimental parameters for S1 and S2, along with PUF coating, epoxy coating, and bare Mg alloy, immersed in an alkaline solution (pH 10). The highest impedance was recorded for S1 (9.0×10^5 kΩ·cm²), indicating superior corrosion resistance, whereas S2 exhibited the lowest impedance (2×10^5 kΩ·cm²). The larger capacitive loop diameter of S1 further confirms its enhanced barrier properties [66]. Similarly, Figure 11(b) presents the impedance characteristics of S3 and S4, where S3 displayed the highest impedance (1.8×10^5 kΩ·cm²), while S4 exhibited the lowest (5.5×10^4 kΩ·cm²). The larger capacitive loop of S3 indicates its superior corrosion resistance. Likewise, Figure 11(c) reveals the impedance behavior of S5 and S6, where S5 demonstrates a higher impedance value (70 kΩ·cm²) compared to S6 (50 kΩ·cm²), indicating better corrosion protection. The observed impedance trends across the samples indicate that the multilayer smart coatings significantly enhance the barrier effect, with S1 and S3 exhibiting the most effective corrosion resistance due to their higher charge transfer resistance. These findings align with recent studies on pH-responsive smart coatings containing multilayer microcapsules [67], which demonstrated that higher pH conditions accelerate inhibitor release, influencing the coating's long-term protective performance. The presence of two semicircles in S3 further supports the hypothesis of a dual-layer corrosion protection mechanism, as previously reported in self-healing polymer-based coatings [30]. The comparative impedance results highlight the critical role of coating integrity and inhibitor release kinetics in maintaining corrosion resistance under alkaline conditions [68,69].

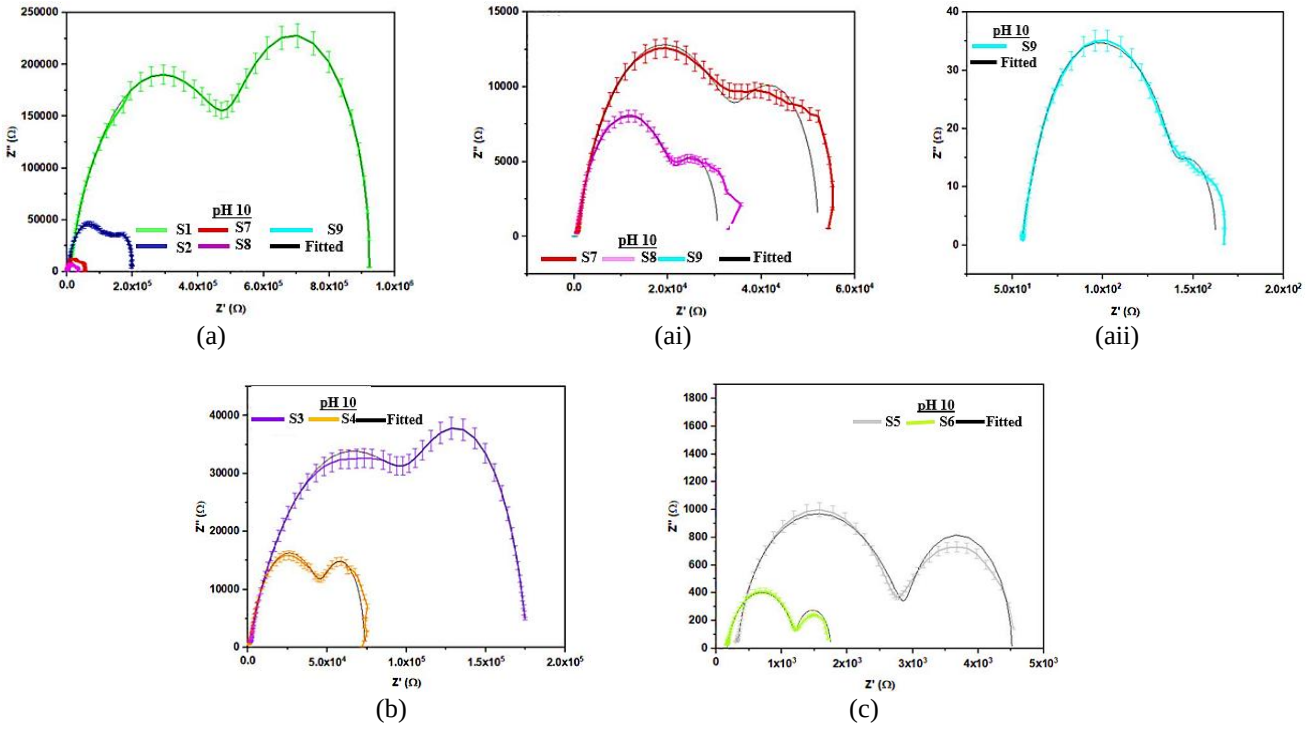

Figure 11. The Nyquist plot of the coated sample in pH 10 (a) S1, S2, S7, S8, S9, (ai) magnified Nyquist plot of S7 and S8, (aii) magnified Nyquist plot of S9, (b) S3 and S4, (c) S5 and S6

4. CONCLUSIONS

This study has demonstrated that pH-responsive multilayer microcapsules are effective in preventing the active corrosion of the AZ31 Mg alloy. The prepared multilayer smart coatings, loaded with benzotriazole (BTA) as a corrosion inhibitor and linseed oil as a self-healing agent, exhibited pH-induced release behavior. The multilayer chitosan–alginate shells facilitate a synergistic mechanism, combining immediate inhibition and self-healing capabilities over time. Captivating BTA release characteristics are exemplified by the fact that acidic (pH 4) conditions allowed the inhibitive agent to be released, targeting the site of corrosion. At the same time, the microcapsule structure remained stable under alkaline conditions (pH 10), providing long-term protection. Good corrosion protection was also indicated by EIS measurements, in which the polarization resistance (R_{ct}) and coating resistance (R_{coat}) of the smart coatings were significantly increased compared to the conventional epoxy coatings. The incorporation of multilayer polyelectrolyte microcapsules into the coating not only improved the barrier performance of the coating but also endowed it with the capability of self-healing, which effectively reduces the amount of microcracks and the size of localized corrosion. This

performance is consistent with that of other researchers, who have also demonstrated that multilayer microcapsules embedded in an epoxy coating can restore more than 90% of the barrier function after damage, as evidenced by an increasing impedance modulus over time. The results indicate that pH-responsive smart coatings have great potential for long-term protective applications of Mg alloys, owing to their high performance and environmental friendliness. The presented system has potential applications in the automotive, aerospace, and biomedical sectors, where the service life and reliability of lightweight metal structures are crucial. The following steps will involve optimizing the microcapsule formulation and testing its performance under real-world conditions to mitigate the practical unfeasibility.

ACKNOWLEDGEMENTS

The authors would like to acknowledge the Ministry of Higher Education for providing financial support under the Fundamental Research Grant Scheme (FRGS) No. FRGS/1/2019/TK05/UMP/02/5 (University reference RDU1901128) and University Malaysia Pahang for laboratory facilities as well as additional financial support under Internal Research grant PGRS210373

CONFLICT OF INTEREST

The authors declare that they have no conflicts of interest.

AUTHORS CONTRIBUTION

N. S. Mohamed (Conceptualization; Formal analysis; Writing - review & editing;)

J. Alias (Conceptualization; Methodology; Validation; Writing - review & editing; Funding acquisition; Supervision)

N. A. Alang (Writing - review & editing; Funding acquisition)

A. F. Omar (Methodology; Validation)

AVAILABILITY OF DATA AND MATERIALS

The data and materials supporting the findings of this study are available from the corresponding author and can be shared upon reasonable request.

ETHICS STATEMENT

Not applicable

REFERENCES

[1] S. Chen, Z. Huang, M. Yuan, G. Huang, H. Guo, G. Meng, et al., "Trigger and response mechanisms for controlled release of corrosion inhibitors from micro/nanocontainers interpreted using endogenous and exogenous stimuli: A review," *Journal of Materials Science & Technology*, vol. 125, pp. 67–80, 2022.

[2] M. Ali, M. Elsherif, A. Salih, A. Ul-Hamid, M. Hussein, S. Park, et al., "Surface modification and cytotoxicity of Mg-based bio-alloys: An overview of recent advances," *Journal of Alloys and Compounds*, vol. 825, pp. 1-17, 2020.

[3] T. Ramakrishnan, K. R. Karthikeyan, V. Tamilselvan, S. Sivakumar, D. Gangodkar, H. Radha, et al., "Study of various epoxy-based surface coating techniques for anticorrosion properties," *Advances in Materials Science and Engineering*, vol. 2022, pp. 1-8, 2022.

[4] J. Tan, L. Liu, H. Wang, J. Luo, "Advances in anti-corrosion coatings on magnesium alloys and their preparation methods," *Journal of Coatings Technology and Research*, vol. 21, pp. 811–825, 2024.

[5] X. Xing, D. Zhou, E. Tang, S. Liu, X. Chu, X. Xu, et al., "A novel method to control the release rate of halloysite encapsulated Na2MoO4 with Ca2+ and corrosion resistance for Q235 steel," *Applied Clay Science*, vol. 188, pp. 1-10, 2020.

[6] M. Rahmati, K. Raeissi, M. Toroghinejad, A. Hakimizad, and M. Santamaria, "Effect of pulse current mode on microstructure, composition and corrosion performance of the coatings produced by plasma electrolytic oxidation on AZ31 Mg alloy," *Coatings*, vol. 9, pp. 1-19, 2019.

[7] D. Zhang, F. Peng, X. Liu, "Protection of magnesium alloys: From physical barrier coating to smart self-healing coating," *Journal of Alloys and Compounds*, vol. 853, pp. 1-22, 2021.

[8] X. Han, J. Hu, Y. Wang, T. Xiao, W. Xia, Y. Chen, et al., "Facile fabrication and properties of super-hydrophobic MgAl-LDH films with excellent corrosion resistance on AZ31 magnesium alloy," *Frontiers in Materials*, vol. 8, pp. 1–12, 2021.

[9] D. Yan, Y. Wang, J. Liu, D. Song, T. Zhang, J. Liu, et al., "Self-healing system adapted to different pH environments for active corrosion protection of magnesium alloy," *Journal of Alloys and Compounds*, vol. 824, pp. 1-12, 2020.

[10] J. Han, S. Tang, H. San, X. Sun, J. Hu, Y. Yu, "Formation mechanism of calcium phosphate coating on a plasma electrolytic oxidized magnesium and its corrosion behavior in simulated body fluids," *Journal of Alloys and Compounds*, vol. 818, pp. 1-14, 2020.

[11] Z. Jia, P. Xiong, Y. Shi, W. Zhou, Y. Cheng, Y. Zheng, et al., "Inhibitor encapsulated{,} self-healable and cytocompatible chitosan multilayer coating on biodegradable Mg alloy: a pH-responsive design," *Journal of Materials Chemistry*, vol. 4, pp. 2498–2511, 2016.

[12] J. Song, X. Cui, G. Jin, Z. Cai, E. Liu, X. Li, et al., "Self-healing conversion coating with gelatin–chitosan microcapsules containing inhibitor on AZ91D alloy," *Surface Engineering*, vol. 34, pp. 79–84, 2018.

[13] Z. Xie, S. Shan, "Nanocontainers-enhanced self-healing Ni coating for corrosion protection of Mg alloy," *Journal of Materials Science*, vol. 53, pp. 3744–3755, 2018.

[14] C. Ding, Y. Tai, D. Wang, L. Tan, J. Fu, "Superhydrophobic composite coating with active corrosion resistance for AZ31B magnesium alloy protection," *Chemical Engineering Journal*, vol. 357, pp. 518–532, 2019.

[15] Z. Zhang, L. Wang, M. Zeng, R. Zeng, M. Kannan, C. Lin, et al., "Biodegradation behavior of micro-arc oxidation coating on magnesium alloy-from a protein perspective," *Bioactive Materials*, vol. 5, pp. 398–409, 2020.

[16] S. Liu, Z. Li, Q. Yu, Y. Qi, Z. Peng, J. Liang, "Dual self-healing composite coating on magnesium alloys for corrosion protection," *Chemical Engineering Journal*, vol. 424, pp. 1-12, 2021.

[17] G. Chen, B. Jin, Y. Li, Y. He, J. Luo, "A smart healable anticorrosion coating with enhanced loading of benzotriazole enabled by ultra-highly exfoliated graphene and mussel-inspired chemistry," *Carbon*, vol. 187, pp. 439–450, 2022.

[18] S. Farshid, M. Kharaziha, M. Atapour, "A self-healing and bioactive coating based on duplex plasma electrolytic oxidation/polydopamine on AZ91 alloy for bone implants," *Journal of Magnesium and Alloys*, vol. 11, pp. 592–606, 2023.

[19] F. Santos, L. Binder, N. Scharnagl, T. da Conceição, "Sustainable smart coatings of chitosan and LDH loaded with natural inhibitors for corrosion protection of Mg AZ31 alloy," *Colloids and Surfaces A: Physicochemical and Engineering Aspects*, vol. 688, pp. 1-10, 2024.

[20] C. Zhou, Z. Li, J. Li, T. Yuan, B. Chen, X. Ma, et al., "Epoxy composite coating with excellent anticorrosion and self-healing performances based on multifunctional zeolitic imidazolate framework derived nanocontainers," *Chemical Engineering Journal*, vol. 385, pp. 1-17, 2020.

[21] H. Cai, P. Wang, D. Zhang, "Smart anticorrosion coating based on stimuli-responsive micro/nanocontainer: a review," *Journal of Oceanology and Limnology*, vol. 38, pp. 1045–1063, 2020.

[22] X. Huang, M. Sun, X. Shi, J. Shao, M. Jin, W. Liu, et al., "Chemical vapor deposition of transparent superhydrophobic anti-Icing coatings with tailored polymer nanoarray architecture," *Chemical Engineering Journal*, vol. 454, pp. 1-9, 2023.

[23] X. R. Nóvoa, C. Pérez, "The use of smart coatings for metal corrosion control," *Current Opinion in Electrochemistry*, vol. 40, pp. 1-8, 2023.

[24] S. Kumar, H. Singh, N. Gaur, S. Patil, D. Kumar, N. Singh, "Imparting increased corrosion passive and bio-active character to Al2O3 based ceramic coating on AZ91 alloy," *Surface and Coatings Technology*, vol. 383, pp. 1-8, 2020.

[25] V. S. Saji, "Organic conversion coatings for magnesium and its alloys," *Journal of Industrial and Engineering Chemistry*, vol. 75, pp. 20–37, 2019.

[26] T. Matsuda, K. B. Kashi, K. Fushimi, V. J. Gelling, "Corrosion protection of epoxy coating with pH sensitive microcapsules encapsulating cerium nitrate," *Corrosion Science*, vol. 148, pp. 188–197, 2018.

[27] C. Kim, A. I. Karayan, J. Milla, M. Hassan, H. Castaneda, "Smart coating embedded with pH-responsive nanocapsules containing a corrosion inhibiting agent," *ACS Applied Materials and Interfaces*, vol. 12, pp. 6451–6459, 2020.

[28] A. B. M. da Cunha, D. A. Leal, L. R. L. Santos, I. C. Riegel-Vidotti, C. E. B. Marino, "pH-sensitive microcapsules based on biopolymers for active corrosion protection of carbon steel at different pH," *Surface and Coatings Technology*, vol. 402, pp. 1-10, 2020.

[29] X. Song, Y. Chen, H. Sun, X. Liu, X. Leng, "Physicochemical stability and functional properties of selenium nanoparticles stabilized by chitosan, carrageenan, and gum Arabic," *Carbohydrate Polymers*, vol. 255, pp. 1-10, 2021.

[30] D. A. Leal, I. C. Riegel-Vidotti, M. G. S. Ferreira, C. E. B. Marino, "Smart coating based on double stimuli-responsive microcapsules containing linseed oil and benzotriazole for active corrosion protection," *Corrosion Science*, vol. 130, pp. 56–63, 2018.

[31] Y. J. Yang, S. M. Yaakob, N. E. Rabat, M. R. Shamsuddin, Z. Man, "Release kinetics study and anti-corrosion behaviour of a pH-responsive ionic liquid-loaded halloysite nanotube-doped epoxy coating," *RSC Advances*, vol. 10, pp. 13174–13184, 2020.

[32] S. Chen, S. Zhao, M. Chen, X. Zhang, J. Zhang, X. Li, et al., "The anticorrosion mechanism of phenolic conversion coating applied on magnesium implants," *Applied Surface Science*, vol. 463, pp. 953–967, 2019.

[33] W. Wu, F. Zhang, Y. Li, L. Song, D. Jiang, R. C. Zeng, et al., "Corrosion resistance of dodecanethiol-modified magnesium hydroxide coating on AZ31 magnesium alloy," *Applied Physics A: Materials Science and Processing*, vol. 126, pp. 1–11, 2020.

[34] X. Hao, S. Chen, D. Qin, M. Zhang, W. Lia, J. Fan, et al., "Antifouling and antibacterial behaviors of capsaicin-based pH responsive smart coatings in marine environments," *Materials Science and Engineering C*, vol. 108, pp. 1-12, 2020.

[35] A. Ibrahim, I. A. Khalil, M. Y. Mahmoud, A. F. Bakr, M. G. Ghoniem, E. S. Al-Farraj, et al., "Layer-by-layer development of chitosan/alginate-based platelet-mimicking nanocapsules for augmenting doxorubicin cytotoxicity against breast cancer," *International Journal of Biological Macromolecules*, vol. 225, pp. 503–517, 2023.

[36] N. Zheng, L. Qia, J. Liu, J. Lu, W. Li, C. Li, et al., "Microcapsules of multilayered shell structure synthesized via one-part strategy and their application in self-healing coatings," *Composites Communications*, vol. 12, pp. 26–32, 2019.

[37] K. Cao, Z. Yu, D. Yin, L. Chen, Y. Jiang, L. Zhu, "Fabrication of BTA-MOF-TEOS-GO nanocomposite to endow coating systems with active inhibition and durable anticorrosion performances," *Progress in Organic Coatings*, vol. 143, pp. 1-14, 2020.

[38] S. Lang, Q. Zhou, "Synthesis and characterization of poly(urea-formaldehyde) microcapsules containing linseed oil for self-healing coating development," *Progress in Organic Coatings*, vol. 105, pp. 99–110, 2017.

[39] M. C. Rivera, A. C. Pinheiro, A. I. Bourbon, M. A. Cerqueira, A. A. Vicente, "Hollow chitosan/alginate nanocapsules for bioactive compound delivery," *International Journal of Biological Macromolecules*, vol. 79, pp. 95–102, 2015.

[40] M. M. De Villiers, D. P. Otto, S. J. Strydom, Y. M. Lvov, "Introduction to nanocoatings produced by layer-by-layer (LbL) self-assembly," *Advanced Drug Delivery Reviews*, vol. 63, pp. 701–715, 2011.

[41] L. S. Barreto, M. S. Tokumoto, I. C. Guedes, H. G. de Melo, F. Amado, V. R. Capelossi, "Study and assessment of the efficiency of the cocoa bark extracted from the theobroma cacao as an inhibitor of the corrosion of carbon steel in substitution of benzotriazole," *Materials Research*, vol. 21, pp. 1-9, 2018.

[42] M. He, Y. Zheng, J. Shen, J. Shi, Y. Zhang, Y. Xiao, et al., "Chitosan/sodium alginate multilayer pH-sensitive films based on layer-by-layer self-assembly for intelligent packaging," *Journal of Renewable Materials*, vol. 12, pp. 215–233, 2024.

[43] I. Kozina, H. Krawiec, M. Starowicz, M. Kawalec, "Corrosion resistance of MgZn alloy covered by chitosan-based coatings," *International Journal of Molecular Sciences*, vol. 22, pp. 1-16, 2021.

[44] A. Khan, A. Hassanein, S. Habib, M. Nawaz, R. A. Shakoor, R. Kahraman, "Hybrid halloysite nanotubes as smart carriers for corrosion protection," *ACS Applied Materials and Interfaces*, vol. 12, pp. 37571–37584, 2020.

[45] X. Ni, Y. Gao, X. Zhang, Y. Lei, G. Sun, B. You, "An eco-friendly smart self-healing coating with NIR and pH dual-responsive superhydrophobic properties based on biomimetic stimuli-responsive mesoporous polydopamine microspheres," *Chemical Engineering Journal*, vol. 406, pp. 1-14. 2021.

[46] J. Miras, C. Liu, E. Blomberg, E. Thormann, S. Vílchez, J. Esquena, "pH-responsive chitosan nanofilms crosslinked with genipin," *Colloids and Surfaces A: Physicochemical and Engineering Aspects*, vol. 616, pp. 1-10, 2021.

[47] C. Radhakumary, K. Sreenivasan, "Synthesis and evaluation of pH responsive silica-polymer hybrid nano capsules," *Soft Materials*, vol. 9, pp. 347–358, 2011.

[48] L. Chen, Z. Yu, D. Yin, K. Cao, "Preparation and anticorrosion properties of BTA@HNTs-GO nanocomposite smart coatings," *Composite Interfaces*, vol. 28, pp. 1–16, 2021.

[49] A. R. Hoseinzadeh, S. Javadpour, "Formulation of a smart nanocomposite coating with pH-responsive loaded halloysite and investigation of its anticorrosion behaviour," *Bulletin of Materials Science*, vol. 43, pp. 1-10, 2020.

[50] R. Mahmoudi, P. Kardar, A. M. Arabi, R. Amini, P. Pasbakhsh, "The active corrosion performance of silane coating treated by praseodymium encapsulated with halloysite nanotubes," *Progress in Organic Coatings*, vol. 138, pp. 1-13, 2020.

[51] N. Ghavidel, S. R. Allahkaram, R. Naderi, M. Barzegar, H. Bakhshandeh, "Corrosion and wear behavior of an electroless Ni-P/nano-SiC coating on AZ31 Mg alloy obtained through environmentally-friendly conversion coating," *Surface and Coatings Technology,* vol. 382, pp. 1-17, 2020.

[52] M. Ghorbani, H. Ebrahimnezhad-Khaljiri, R. Eslami-Farsani, H. Vafaeenezhad, "The synergic effect of microcapsules and titanium nanoparticles on the self-healing and self-lubricating epoxy coatings: A dual smart application," *Surfaces and Interfaces,* vol. 23, pp. 1-10, 2021.

[53] L. Zhu, C. Peng, K. Kuroda, and M. Okido, "Hydrophilic thin films formation on {AZ}31 alloys by hydrothermal treatment in silicate containing solution and the evaluation of corrosion protection in phosphate buffered saline," vol. 6, pp. 1-12, 2019.

[54] J. Petkovska, N. Geskovski, D. Markovi´c, V. Dimova, D. Mirakovski, M. Radeti´c, et al., "Chitosan-pectin multilayer coating with anthocyanin grape dye as pH indicating wound dressing: Synthesis and characterization," *Carbohydrate Polymer Technologies and Applications,* vol. 7, pp. 1-11, 2024.

[55] A. Khan, A. Hassanein, S. Habib, M. Nawaz, R. A. Shakoor, R. Kahraman, "Hybrid halloysite nanotubes as smart carriers for corrosion protection," *ACS Applied Materials and Interfaces,* vol. 12, pp. 37571–37584, 2020.

[56] H. Ahmadi, V. Haddadi-Asl, H. E. Mohammadloo, "Advancing anticorrosion and antibacterial performance of mg AZ31 implants using novel pH-responsive polymeric surfactant for preparing PLGA nanoparticles," *Surface and Coatings Technology,* vol. 482, pp. 1-15, 2024.

[57] J. Wang, J. Tang, H. Zhang, Y. Wang, H. Wang, B. Lin, et al., "A CO2-responsive anti-corrosion ethyl cellulose coating based on the pH-response mechanism," *Corrosion Science,* vol. 180, pp. 1-15, 2021.

[58] S. Chen, X. Li, Z. Yang, S. Zhou, R. Luo, M. F. Maitz, et al., "A simple one-step modification of various materials for introducing effective multi-functional groups," *Colloids and Surfaces B: Biointerfaces,* vol. 113, pp. 125–133, 2014.

[59] S. Chen, J. Zhang, Y. Chen, S. Zhao, M. Chen, X. Li, et al., "Application of phenol/amine copolymerized film modified magnesium alloys: Anticorrosion and surface biofunctionalization," *ACS Applied Materials and Interfaces,* vol. 7, pp. 24510–24522, 2015.

[60] L. Cheng, C. Liu, H. Wu, H. Zhao, F. Mao, L. Wang, "A mussel-inspired delivery system for enhancing self-healing property of epoxy coatings," *Journal of Materials Science and Technology,* vol. 80, pp. 36–49, 2021.

[61] Y. Ye, H. Chen, Y. Zou, H. Zhao, "Study on self-healing and corrosion resistance behaviors of functionalized carbon dot-intercalated graphene-based waterborne epoxy coating," *Journal of Materials Science and Technology,* vol. 67, pp. 226–236, 2021.

[62] C. Wang, H. Fang, X. Qi, C. Hang, Y. Sun, Z. Peng, et al., "Silk fibroin film-coated MgZnCa alloy with enhanced in vitro and in vivo performance prepared using surface activation," *Acta Biomaterialia,* vol. 91, pp. 99–111, 2019.

[63] C. Zhou, H. Zhang, X. Pan, J. Li, B. Chen, W. Gong, et al., "Smart waterborne composite coating with passive/active protective performances using nanocontainers based on metal organic frameworks derived layered double hydroxides," *Journal of Colloid and Interface Science,* vol. 619, pp. 132–147, 2022.

[64] Q. Luan, H. Zhang, J. Wang, Y. Li, M. Gan, Q. Deng, et al., "Electrostatically reinforced and sealed nanocellulose-based macrosphere by alginate/chitosan multi-layer coatings for delivery of probiotics," *Food Hydrocolloids,* vol. 142, pp. 1-9, 2023.

[65] M. Azadi, S. Dezianian, M. Azadi, A. H. Beyzavi, V. Talebsafa, "Effects of various adhesive layers on electrochemical characteristics of 3D-printed polylactic acid coatings on AM60 magnesium alloy," *High Temperature Corrosion of Materials,* vol. 101, pp. 433-454, 2023.

[66] S. Y. Jian, C. Y. Yang, J. K. Chang, "Robust corrosion resistance and self-healing characteristics of a novel Ce / Mn conversion coatings on EV31 magnesium alloys," *Applied Surface Science,* vol. 510, pp. 1-15, 2020.

[67] C. Sun, C. Liu, Y. Wang, D. Jiao, A. M. Zhang, P. S. Sui, et al., "Corrosion sensing and self-healing composite coatings on magnesium alloy AZ31 enabled by stimuli-responsive microcapsules loaded with phenolphthalein and epoxy resin," *Progress in Organic Coatings,* vol. 186, pp. 1-13, 2024.

[68] C. Li, X. Guo, G. S. Frankel, "Smart coating with dual-pH sensitive, inhibitor-loaded nanofibers for corrosion protection," *npj Materials Degradation,* vol. 5, pp. 1-13, 2021.

[69] P. Xie, Y. He, F. Zhong, C. Zhang, C. Chen, H. Li, et al., "Cu-BTA complexes coated layered double hydroxide for controlled release of corrosion inhibitors in dual self-healing waterborne epoxy coatings," *Progress in Organic Coatings,* vol. 153, pp. 1-14, 2021.